Effect of Y-doped TiO_2(B)/SnO_2 1D structured nanocomposite on the performance and capacity of lithium-ion batteries

P. Choopool[a,b], V. Rachpech[a,b,*], M. Khangkhamano[a,b]
[a]*Center of Excellence in Metal and Materials Engineering (CEMME), Faculty of Engineering, Prince of Songkla University, 90112, Songkhla, Thailand*
[b]*Department of Mining and Materials Engineering, Faculty of Engineering, Prince of Songkla University, 90112, Songkhla, Thailand*

Because traditional graphite anode for Lithium-ion batteries (LIBs) has low coulombic efficiency, high irreversible capacity and large volume expansion which can no longer satisfy the requirements of high-performance batteries. This article therefore presented the development of an anode material based on structural design to enhance its properties. One-dimension structured nanocomposites of yttrium-doped TiO_2(B) nanowires/ SnO_2 nanotubes were synthesised at various yttrium concentrations via hydrothermal method. Phase composition, crystal structure, morphologies, and electrochemical properties were evaluated to study the effects of the dopant on performance and capacity of the LIBs. XRD showed the modification in crystalline size and lattice parameters when yttrium was introduced. Electrochemical properties were markedly enhanced by the yttrium-doped nanocomposites, especially for the one with 0.5%mole yttrium (TSY50). The TSY50 offered the highest diffusion coefficient of 2.34×10^{-10} cm^2/s, reduced the Li-ion diffusion length and the cell resistance, improved the specific capacity, cycle performance and capacity retention, as demonstrated by cycling tests. The prepared yttrium-doped nanocomposite could be considered as a promising material for its application as an anode in LIBs.

(Received June 13, 2022; Accepted February 10, 2023)

Keywords: Yttrium, TiO_2(B), SnO_2, Nanowires, Nanotubes, Lithium-ion batteries

1. Introduction

As a green power supply, Lithium-ion battery (LIBs) has attracted much attention in recent years due to its high energy density, long life cycle and low self-discharge. LIBs are widely used in many applications such as portable electronic devices and tools, mobile devices, and electric vehicles [1, 2]. However, traditional electrode materials, commercial graphite, for LIBs can no longer meet the growing demand for high-performance batteries. This is because the traditional graphite anode has the theoretical capacity of 370 mAh/g [1] resulting in low coulombic efficiency, high irreversible capacity and large volume expansion [2]. The development of anode materials with higher capacity, faster-charging speed, and more extended cycle performance, therefore, has become one of the current research trends.

A number of anode materials have been studied to improve the electrochemical properties for a higher performance battery, including TiO_2, SnO_2, SnO_x/TiO_2, TiO_2/MoO_3, $Li_4Ti_5O_{12}$, and MoS_2 [1, 2]. As an anode material for LIBs, although TiO_2 has a remarkable reversible capacity, high chemical/thermal stability, safe reaction potential (>1.5 V *vs.* Li/Li^+), small volume change, environmental friendliness, and excellent cycle performance [2], its low theoretical specific capacity (175-335 mAh/g) and poor electric and ionic conductivities [2] limit the application in the field of power batteries.

To overcome its drawbacks, in this study, four strategies have been proposed: (i) fabrication of one-dimension nanostructures; (ii) the use of bonze-phase titanium oxide (TiO_2(B)); (iii) compositing with SnO_2; and (iv) doping with yttrium (Y). Strategy (i), a high surface area is

* Corresponding author: rvishnu@eng.psu.ac.th
https://doi.org/10.15251/DJNB.2023.181.211

concerned as to increase contact area between the active materials and the electrolyte and hence 1D nanostructures (nanowires and nanotubes) are fabricated here. Hua *et al.* [3] reported that long length TiO_2(B) nanorod solid state LIBs had a high cycle performance, which the Li^+ could be easily transported along the length compared to the TiO_2 (P25) nanoparticles. Wang *et al.* [4] reported that porous SnO_2 nanotubes fabricated by microwave-assisted hydrothermal process had a high surface area for oxidation-reduction reactions because of high Li^+ storage capacity and great cyclic performance. Wu *et al.* [5] claimed that SnO_2 flower-like structure showed the advantage for Li^+ transport with short length for ion diffusion due to the high reversible reaction in anode cell of LIBs. Strategy (ii) TiO_2(B) is chosen here because this low-density phase provides the highest capacity (200-300 mAh/g) and a more open tunnel structure compared with other polymorphs (anatase, rutile, and brookite) which enhances ion transport and cycles performance [2, 6]. Wu *et al.* [7] prepared TiO_2(B) nanosheets by hydrothermal process and found that their electrochemical properties were highly reversible capacity, good cycling stability with excellent capacity after 25 cycles, and effectively buffer the volume changes during ion transport. Strategy (iii) the combination of TiO_2(B) nanowires with SnO_2 nanotubes here is to improve the Li^+ storage capacity and cyclability of SnO_2-based anodes. Because bulk TiO_2 has low capacity and poor electrical conductivity while SnO_2 possesses high electrical conductivity, high theoretical specific capacity (782 mAh/g) but poor cycle performance and low working voltage (0.6 V *vs.* Li/Li^+) [1, 2]. Furthermore, it was found that SnO_2 nanoparticles coated on TiO_2(B) nanosheets offered high discharge capacity, great cycle performance, and coulomb efficiency ~93.1% [7]. However, excess SnO_2 decreased the capacity retention due to Li-Sn composite formation and volume extension [8]. SnO_2 exhibits a volume changes as much as 200% during charge/discharge cycling, affecting the cycle life and performance of the LIBs. Thus, the use of nanostructured TiO_2(B)/SnO_2 composites can improve the Li^+ storage capacity and cyclability of SnO_2-based anodes because of the mechanical support function of the TiO_2(B) during the charge/discharge cycling [1]. Strategy (iv) doping the nanocomposite with Y is to enhance electron injection efficiency, and reduce electron trapping and transport time. Aghazadeh *et al*. [9] studied the effect of Y-doped Fe_2O_3 by cathodic electrodeposition method on supercapacitor ability and found that Y^{3+} dopant enhanced the ability up to 20%. Furthermore, Qu *et al*. [10] and Baig *et al.* [11] reported that Y-doped TiO_2 is helpful for oxygen vacancy formation which is used in gas production and solar cell application. Khan *et al*. [12] synthesised TiO_2 nanorods doping with Y^{3+} ions which is used for H_2 production under visible light. Y doping reduced the bandgap energy and induced the mixed-phase formation of anatase/rutile resulting in a high photocatalytic activity for H_2 generation.

In this article, based on the above structural design, the influence of Y-doped TiO_2(B) nanowires/SnO_2 nanotubes on electrochemical properties was investigated. The nanomaterials were prepared via hydrothermal method with various Y concentrations. The fabrication, characterization, microstructure, and electrochemical performance of the prepared TiO_2(B)/SnO_2 nanomaterial electrodes were reported and discussed.

2. Experimental

2.1. Synthesis of Manganese oxide nanowires and Tin oxide nanotubes [13, 14]

Manganese oxide nanowires (MnO_2 NWs) were fabricated by 0.264 g potassium permanganate ($KMnO_4$, Ajax Finchem) mixed in 30 ml distilled water. After stirring for 20 min, 0.4 ml hydrochloric acid (96% HCl, J.T. Baker) was added to the mixture and continually stirred for 20 min. Next, the solution was transferred to a Teflon-line autoclave and annealed at 200°C for 12h. Then, the reacted product was filtered and washed until pH ~7 by water and ethanol. The powder was dried in an oven at 95°C for 24h.

Tin oxide nanocrystals (SnO_2) were coated on MnO_2 NWs template. First, 0.10 g MnO_2 NWs was added to 30 ml distilled water and stirred at room temperature for 30 min. Next, 0.10 g of stannous chloride ($SnCl_2.2H_2O$, Ajax Finchem) and 0.5 ml HCl (96%, J.T. Baker) were added while stirring. After that, the mixture was transferred to autoclave and annealed at 200°C for 4h. Then, the MnO_2/SnO_2 precipitate was filtered and washed until pH ~7 by water and ethanol. The

powder was collected and dried in an oven at 95°C for 24h. Finally, SnO_2 NTs were obtained by removing the template with oxalic acid. The 0.1g of powder was transferred to 30 ml sulfuric acid solution (30% H_2SO_4) at 60°C, added 0.2 g oxalic acid ($C_2H_2O_4$, Kemaus), and stirred for 30 min. The powder was filtered and washed until pH ~7 by water and ethanol. Then, it was dried in an oven at 95°C for 24h, annealed at 400°C for 2h.

2.2. Synthesis of Titanium dioxide phase B nanowires

Titanium dioxide (phase B) nanowires (TiO_2(B) NWs) were fabricated by hydrothermal method. 1.0 g of TiO_2 powder (Degussa P25) was mixed with 30 ml of 10 M sodium hydroxide (NaOH, Kemaus) and sonicated at room temperature for 1h. Next, the mixture was transferred to an autoclave and annealed at 220°C for 24h. Then, the precipitate was collected, washed with 0.1 M HCl, water, and ethanol until pH ~7. After that, the product was dried at 95°C for 24h and annealed at 400°C for 2h.

2.3. Synthesis of Yttrium-doped Titanium dioxide phase B nanowires/Tin oxide nanotubes

Yttrium-doped Titanium dioxide phase B nanowires/Tin oxide nanotubes (TSY) were prepared by hydrothermal method. First, 1:1 TiO_2(B) NWs:SnO_2 NTs powder was mixed in 30 ml of 1:1 ethanol:water and stirred for 20 min at room temperature. Next, Yttrium precursor, Yttrium nitrate ($Y(NO_3)_3$, 99.8%, Sigma-Aldrich) was added into the solution varied at 0-1%mole of Ti. Then, 1 ml HCl was added and stirred for 20 min at room temperature. After that, the dispersion was transferred to an autoclave and annealed at 95°C for 6h. Finally, the precipitate was collected, washed with water until pH ~7 and dried at 95°C for 24h.

All synthesized samples were labeled according to their synthesis conditions and listed in Table 1.

Table 1. Lists of samples and their synthesis conditions.

Sample ID	Details
T	Pure TiO_2 (B) NWs
S	Pure SnO_2 NTs
TS	TiO_2(B) NWs/SnO_2 NTs
TSY25	TiO_2(B) NWs/SnO_2 NTs with 0.25% mole Y: TiO_2(B)
TSY50	TiO_2(B) NWs/SnO_2 NTs with 0.50% mole Y: TiO_2(B)
TSY1	TiO_2(B) NWs/SnO_2 NTs with 1.00% mole Y: TiO_2(B)

2.4 Materials characterization

The degree of crystallinity and phase composition of as-synthesized nanopowders were studied by X-ray diffractometer (XRD; Philips X'Pert MPD, United Kingdom) with CuKα (λ=1.5405 Å) radiation at 40 kV in the 2θ-range 5°−90° with scan rate 0.05°/s. The lattice parameters (*a*, *b* and *c*) of TiO_2(B) and SnO_2 were calculated from XRD results using d-spacing and the standard formula for different crystal systems [15]. The crystallite size (*D*, nm) was also estimated from the highest XRD peaks of TiO_2(B) and SnO_2 using Scherrer's formula, equation (1):

$$D = 0.9\lambda/\beta\cos\theta \quad (1)$$

where λ is the x-ray wavelength (nm), β is the peak full width at half maximum (FWHM), and θ is the Bragg angle.

The morphology and topography of the nanoscale powder were examined using field-emission scanning electron microscopy (FE-SEM; Apreo FEI, USA) at an accelerating voltage of 5 kV and transmission electron microscopy (TEM; JEOL 2010, Japan) at 200 kV. The elemental

composition was also analyzed using the energy dispersive X-ray spectroscopy (EDS; Oxford Instruments, United Kingdom) at 20 kV.

2.5 Electrochemical measurement

The anode electrode was fabricated by mixing the as-synthesised materials, carbon black powder (N330), and polyvinylidene fluoride (PVDF, Alfa aesar) in n-methyl-2-pyrrolidone solution (99.8% NMP, Loba chemis) at a ratio of 80:10:10. The mixture was stirred and coated on a copper plate. After being dried on a hot plate at 60°C, the electrode was annealed in a vacuum oven at 90°C for 12h. The electrochemical properties were investigated using electrochemical impedance spectroscopy (EIS), Metrohm Autolab. The cyclic voltammetry (CV) was measured by using a three-electrode electrochemical cell method in a 0.1 M Lithium carbonate (Li_2CO_3, Mallinckrodt) electrolyte. Coated materials on a copper plate (1.0×1.0 cm^2), Ag/AgCl, and platinum (Pt) wire were used as working, reference, and counter electrodes, respectively. The potential windows were run at −0.6 to +0.6 V with a scanning rate of 0.05 V/s. Then, the result was collected and analyzed.

Diffusion coefficient (D_0, cm^2/s) of Li^+ in the electrode was calculated from CV curve by following equation [16]:

$$i_p=(2.69\times10^5)n^{3/2}AD_0^{1/2}C_0v^{1/2} \quad (2)$$

where i_p is the current intensities at highest position (A/g), n is the electron transfer number, A is apparent surface area (cm^2/g), C_0 is the maximum ion concentration ($mole/cm^3$), and v is the sweep rate.

The schematic of LIBs cell was illustrated in Fig 3(a). As-synthesised nanocomposite coating on a copper plate (1.5×1.5 cm^2) was used as an anode while a lithium plate (99.9% Li, Alfa aesar) was employed as a cathode electrode. Polypropylene paper (Celgard® 2400) was used as a separator. An electrolyte was a solution of 1.0 M lithium hexafluorophosphate in ethylene carbonate and diethyl carbonate ($LiPF_6$ in EC/DC 1:1, Alfa aesar). All components were then assembled in a homemade box under argon gas (O_2 < 100 ppm). The impedance and the charge-discharge measurement were then recorded. The impedance was carried out between 0.1 to 10^5 Hz with an amplitude of 10 mA at room temperature. The galvanostatic charge-discharge was performed at a cycle potential window between 0.1 to 4.2 V and a current of 1 mA.

3. Results and Discussion

3.1. Phase composition and crystal structure

Figure 1 shows XRD patterns of as-synthesised nanomaterials: the single oxide (a) T (TiO_2(B)), the nanocomposite (b) TS (TiO_2(B)/SnO_2), and the Y-doped nanocomposites (c-e) TSY (Y-doped TiO_2(B)/SnO_2) at (c) 0.25, (d) 0.5, and (e) 1 mol%Y. The T (Fig1A(a)) exhibits only monoclinic phase of TiO_2(B) at 2θ = 14.5, 24.9, 28.9, 44.4 and 48.4 degrees corresponding to plan (200), (110), (002), (003), and (020), respectively (JCPDS no. 74-1940). The TS (Fig.1A(b)) shows a combination of the TiO_2(B) and the rutile tetragonal structure of *o*-SnO_2. The *o*-SnO_2 peaks were observed at 2θ = 26.6, 33.8, 38.3 and 51.9 degrees corresponding to plan (110), (101), (200) and (211), respectively (JCPDS no. 41-1445). For the TSY at all Y concentrations (Fig.1A(c-e)), only the diffraction peaks of TiO_2(B) and the *o*-SnO_2 was found with no sign of additional characteristic peaks (such as Y_2O_3) which may be attributed to the low Y content. Although that, Y-doping effects were observed on the diffraction peak characteristics as the peak intensity and position were modified. Fig.1B illustrates the extended XRD patterns of all samples from 2θ = 10 to 35 degrees. As compared to the TS (Fig. 1B(b)), the TSY (Fig.1B(*c*-*e*)) showed lower TiO_2(B) peak intensities at 2θ = 14.2 and 25.0 degrees, as the Y concentration increased, and peak-shifts to lower diffraction angles from 2θ = 14.2 to 14.0 degrees and from 2θ = 25.0 to 24.8 degrees. Not only that but also lattice parameters of the TiO_2(B), in particular *a*, were

modified when Y was introduced (see Table 2). These phenomena were attributed to Y interstitials in the TiO_2(B) structure because the interstitial Y^{3+} (0.90 Å) has a larger ionic radius than Ti^{6+} (0.75 Å) and Sn^{4+} (0.69 Å) resulting in lattice distortion and the modified lattice parameters. Also, this may lead to an increase in oxygen vacancies and defects in the structure and hence the observation of modified peak intensities and positions [10-12]. In addition, the crystallite size of TiO_2(B) calculated from Eq. 1 increased with doping concentration from about 9.9 nm (the T and the TS) to 15.9 nm (the TSY1) as demonstrated in Table 2. This suggested the effects of Y doping on crystallinity that Y doping promoted grain growth and lattice distortion.

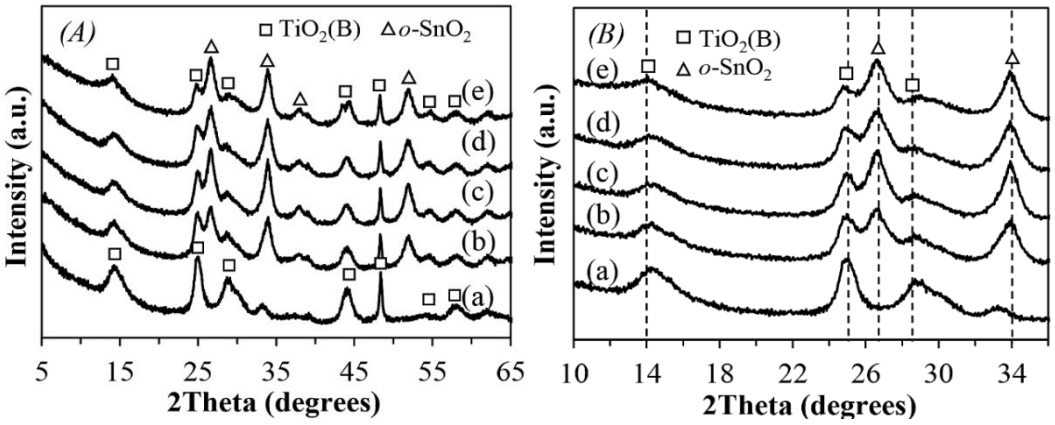

Fig. 1. (A) XRD result and (B) XRD extended at 2θ = 10 to 35 degrees of (a) TiO_2(B) NWs (T), (b) TiO_2(B) NWs/SnO_2 NTs (TS), Y-doped TiO_2(B) NWs/SnO_2 NTs (TSY) at (c) 0.25, (d) 0.5 and (e) 1 %mole.

Table 2. The lattice parameters of TiO_2 and SnO_2 in the Y-doped nanocomposites.

Sample	Lattice parameters (Å)						Crystallite size (nm)	Diffusion coefficient ($\times 10^{-10}$cm^2/s)	Series resistance (Ω)
	TiO_2(B)				SnO_2				
	a	*b*	*c*		*a, b*	*c*			
T	13.02	3.76	6.50		-	-	9.9	0.13	22.5
S	-	-	-		4.73	3.16	9.2	63.32	-
TS	13.10	3.77	6.52		4.74	3.19	9.9	1.75	8.8
TSY25	13.06	3.77	6.50		4.74	3.18	9.9	1.11	8.6
TSY50	13.14	3.77	6.51		4.74	3.18	11.4	2.34	5.4
TSY1	13.18	3.77	6.49		4.74	3.19	15.9	0.32	4.6

3.2 Morphologies

Figure 2 demonstrates the morphologies of as-synthesised nanostructures. The pure TiO_2(B) (Fig. 2(a)) exhibited nanowire structure with smooth surfaces that agglomerate forming bundles of 1D nanostructure. The average diameter and length of the nanowires were 100 nm and 3 µm, respectively. Fig. 2(b-c) show microstructure of the doped sample; TSY50. Clearly, the TSY50 demonstrated composite 1D nanostructures of the TiO_2(B) nanowires and SnO_2 nanotubes (indicated by the red circle). The nanotubes were found to be agglomerated (Fig.2(b)) with rough surfaces due to the formation of SnO_2 nanocrystals while the nanowire surfaces were composed of dispersed nanocrystals (Fig.2(c)). The nanotube structure was further magnified by TEM (Fig.2(d)) providing further insight into the morphology and microstructure of the material. The result further confirms that the nanotubes were made up of agglomerated SnO_2 nanoparticles with

an average particle size of about 10 nm. The inner tube diameter was about 65.2 nm and the wall thickness was 8.2 nm. This suggested that SnO_2 nanoparticles formed uniformly on the template surfaces (MnO_2 nanotubes). Once the template (the core) was removed, nanotube structure with rough surface due to the deposition of SnO_2 nanoparticles was therefore obtained.

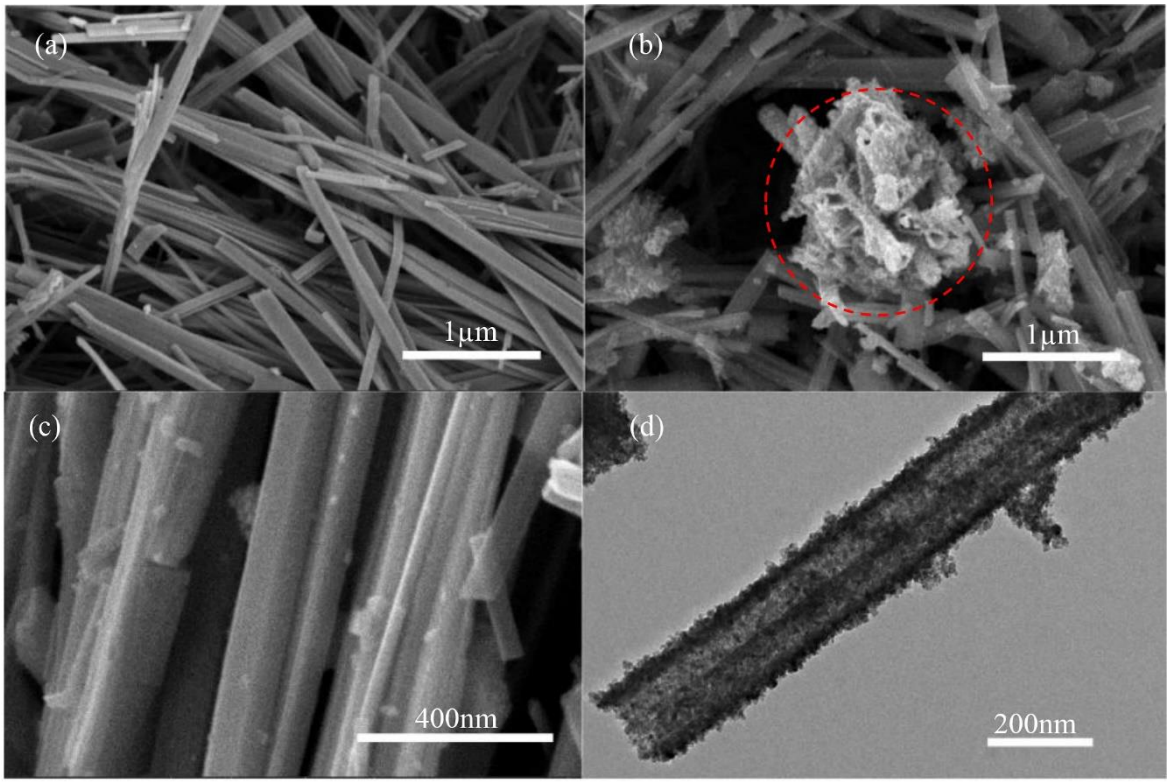

Fig. 2. FE-SEM images of (a) TiO_2(B) NWs (T), (b-c) Y-doped TiO_2(B) NWs/SnO_2 NTs at 0.5%mole Y (TSY50), and (d) TEM image of SnO_2 NTs (S).

3.3. Electrochemical properties of the nanocomposites as LIBs anodes

The cyclic voltammetry (CV) test was applied to study electrochemical performance of the nanomaterials using a voltage window between −0.6 V and +0.6 V in a 0.1 M Li_2CO_3 electrolyte. Figure 3(a) presents the first twenty-five CV curves for the undoped (T and TS) and Y-doped nanomaterials (TSY25, TSY50, and TSY1). The resulting CV showed two different regions of anodic (positive current values) and cathodic (negative current values) peaks where the oxidation and reduction take place, respectively. As expected, a small oxidation/reduction peak was noticed on the T, indicating its poor reversibility in electrochemical reaction. Interestingly, the largest oxidation/reduction peak was found on the TSY50, pointing out a highly reversible electrochemical reaction of the Y-doped nanocomposite anode. Furthermore, the highest redox activity gained from the TSY50 at +0.016 V and −0.39 V corresponds to the deintercalation and intercalation (see Eq. (3-5)) of Li^+. These reactions led to capacity loss during the first charge-discharge process [17, 18]. Generally, the reversible reactions (Eq. (3) and (5)) were the alloying/de-alloying process during Li^+ transport. It is worth to noting that although SnO_2 electrode offers high capacity, the formation of Li_xSn (Eq. (5)) causes volume extension of the electrode resulting in battery degradation and short-term service [18, 19]. Note that excess Y (>0.5%mol, the TSY1) yielded a small oxidation/reduction peak, suggesting a significant decrease in electrochemical performance of the electrode. This may be attributed to an excess defect concentrations and oxygen vacancies as well as excess formation of Y_2O_3 on the surfaces of nanowires/nanotubes which inhibit Li^+ ions transport [8, 20]. Furthermore, the deintercalation and intercalation gained from the TSY50 was considerably increased as the number of cycles increased (Fig.3b). This pointed out a high Li^+ transport capability when the charge-discharge voltage was

applied as a result of Y dopant. The electrochemical reactions of Li^+, TiO_2(B), and SnO_2 can be described by the following reactions (3-5) [17-22]

$$TiO_2 + xLi^+ + xe^- \leftrightarrow Li_xTiO_2 \qquad (0 \le x \le 1) \qquad (3)$$

$$SnO_2 + 4Li^+ + 4e^- \rightarrow Sn + 2LiO_2^+ \qquad (4)$$

$$Sn + xLi^+ + xe^- \leftrightarrow Li_xSn \qquad (0 \le x \le 4.4) \qquad (5)$$

To analyse the influence of Y doping on Li^+ diffusion, the diffusion coefficient (D_0) of doped nanocomposites was calculated from CV curves using Eq. (2) and displayed in Fig. 3(c). The T, undoped anode, showed the lowest D_0 of 0.13×10^{-10} cm^2/s. The diffusion coefficient increased to 1.75×10^{-10} cm^2/s when TiO_2 and SnO_2 were combined (the TS). The effect of Y on D_0 can be seen clearly when the D_0 reached the highest value of 2.34×10^{-10} cm^2/s at 0.5%mole Y (TSY50). The D_0, however, decreased dramatically to 0.32×10^{-10} cm^2/s when 1%mole Y (TSY1) was applied. This could be a result of excess defects and oxygen vacancies in the structures, resulting in a charge ion being trapped in the structures and thus poor ion exchange of the materials [20]. Furthermore, excess Y_2O_3 coating on the nanostructured surfaces may be formed which prevented Li^+ ions insertion/extraction through 1D nanomaterials [20, 22]. Note that the estimated D_0 values were in accordance with the CV testing results that TSY50 yielded the highest electrochemical performance while the lowest one was the T. As compared to the T and TS anodes, the enhancement in the diffusion coefficient, charge transfer, and the reversible reactions could be ascribed to the optimum Y doping on TiO_2(B)/SnO_2 nanocomposites.

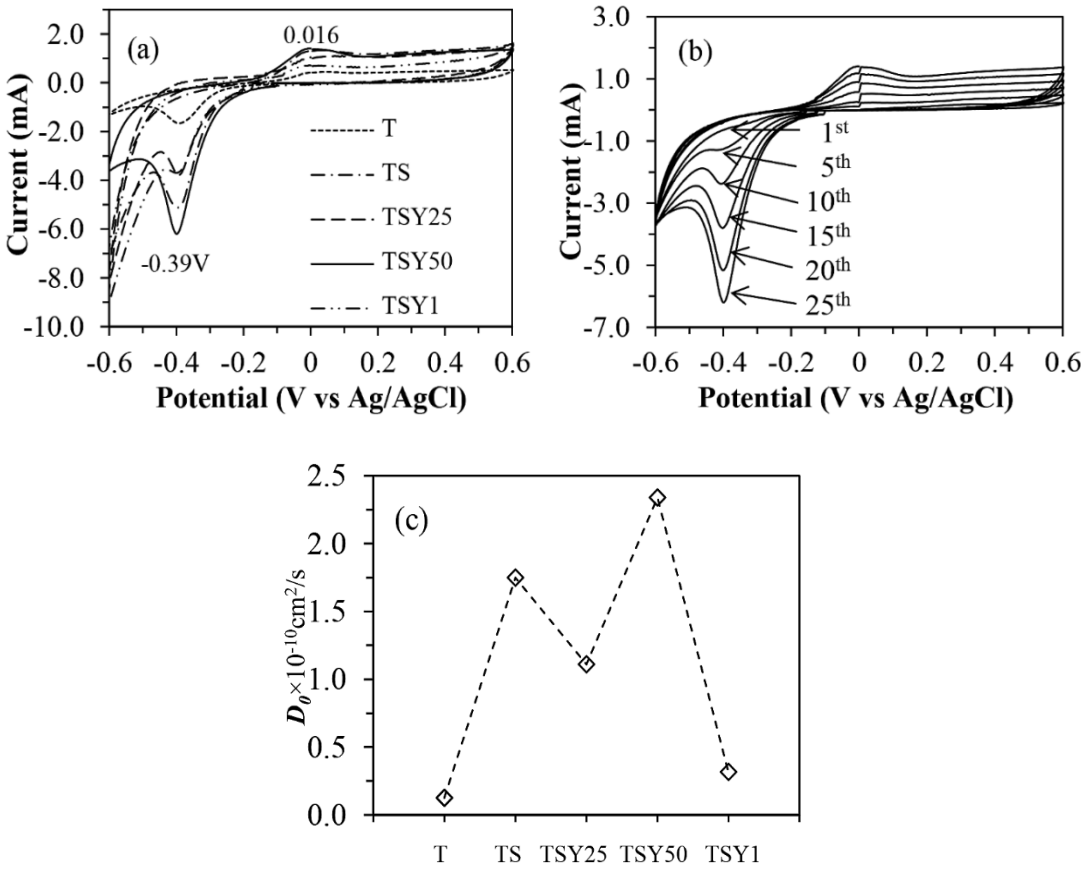

Fig. 3 (a) CV results at 25th cycles of TiO_2(B) NWs (T) TiO_2(B) NWs/SnO_2 NTs (TS) and Y doped TiO_2(B) NWs/SnO_2 NTs at difference amount of %mole Y; 0.25 (TSY25), 0.50 (TSY50) and 1%mole (TSY1); (b) CV results after 25th cycles of the TSY50; and (c) Diffusion coefficient (D_0) after 25th cycles of all samples.

To investigate the electrochemical performance of the prepared nanomaterials, LIBs cells were assembled. Figure 4 illuminates schematic of the LIBs cell which the nanomaterials were used as LIBs anodes. The Nyquist plots were conducted to examine impedance of LIBs. Figure 5(a) presents a series of Nyquist plots of the prepared nanomaterials. Clearly, the plots consisted of semi-circle and linear zones. The size of semi-circle represents the charge transfer resistance and charge recombination resistance of the nanomaterial-electrolyte interface [23]. For the undoped samples (T and TS), their semi-circles were large which attributed to a large charge transfer resistance. The size of semi-circle, however, decreased as the anode material was further doped with Y, suggesting the smaller resistances in charge transfer and charge recombination of the doped samples. Interestingly, among them, the TSY50 exhibited the smallest semi-circle, and hence its lowest charge transfer resistance. The inset (Fig.5(a)) shows the impedance of the cell that shifted to the origin when Y was doped. The shifted impedance of the real part on the x-axis represents the decreased series resistance with the increased Y concentration. Here, the TSY50 LIBs had the series resistance approximately 5.4 Ω which was markedly lower than that of the undoped T (22.5 Ω) and TS (8.8 Ω) anodes. Therefore, the decrease in size of the semi-circle and increase in charge transfer capability, as well as the left-shifted impedance of the doped materials with the increased Y suggested the effects of Y dopant on the electrochemical performance. Note that the low series resistance and decreased ion transfer resistance of the TSY50 led to enhanced electrical conductivity, ion transport across electrolyte-electrode interfaces and hence superior cycle performance of the LIBs.

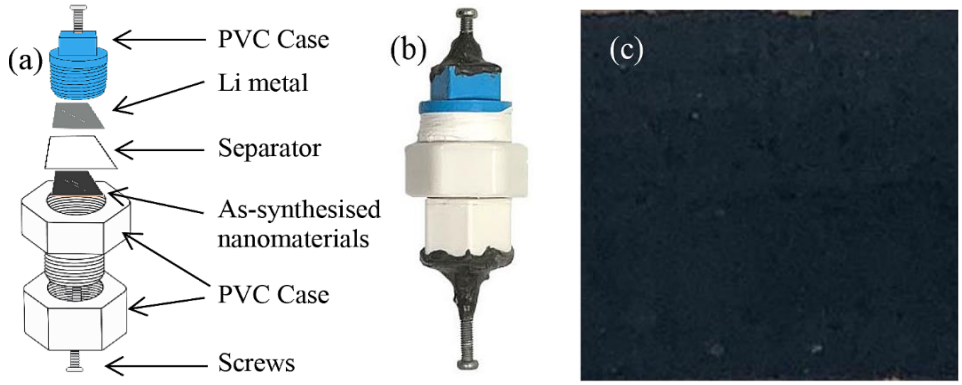

Fig. 4. (a) Schematic diagram and (b) photographs of TSY50 LIBs cell and (c) TSY50 coated on a copper plate.

Figure 5(b) shows the galvanostatic charge-discharge curves for the TSY50 sample. The first specific charge/discharge capacity was 1,416.7/944.0 mAh/g, while that for the third cycle were decreased to 1,393.7/684.5 mAh/g. In comparison with the TSY50, the undoped TS exhibited a much lower specific charge/discharge capacity of 821.1/719.1 mAh/g for the 1st cycle and 749.1/516.2 mAh/g for the 3rd cycle. Furthermore, the specific discharge capacity and capacity retention of the TSY50 and TS calculated from the specific discharge capacity were illustrated in Fig. 5(c). The capacity retentions of TSY50 and TS at the 3rd cycle was 81.3% and 75.9% in Fig. 5(d), respectively. After 40 cycles, the capacity decreased to 219.7 mAh/g and 118.8 mAh/g for the TSY50 and TS, respectively, along with the capacity retention of 22.6% and 16.5%, respectively. This suggests the decrease of electrode polarization due to the formation of solid electrolyte interphase (SEI) film, composite materials, and irreversible process between Li^+ charge-discharge in Eq. (5) [16-18].

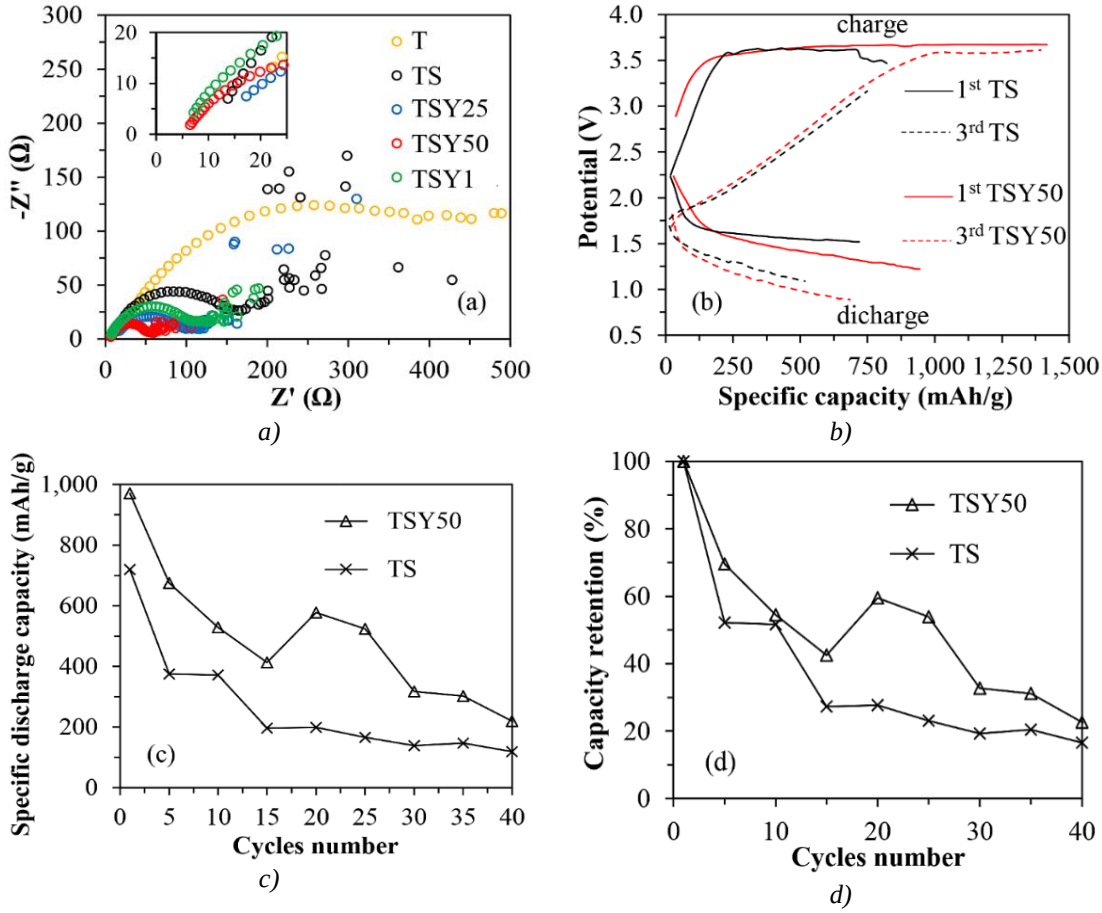

Fig. 5. (a) Nyquist plots, (b) galvanostatic charge-discharge profiles at 1 and 3 cycles, and (c) Specific discharge capacity at 1-40 cycles and (d) Capacity retention of TSY50 at a current of 1 mA of TiO_2(B) NWs/SnO_2 NTs (TS) and Y-doped nanocomposites as anode cell of LIBs.

4. Conclusions

Y-doped TiO_2(B)/SnO_2 1D-structured nanocomposites were prepared and used as anode materials for LIBs. The effect of Y doping on electrochemical performance was explored and investigated in comparison with the undoped anodes; the TiO_2 nanowires, the SnO_2 nanotubes, and the TiO_2(B)/SnO_2 nanocomposites. Both doped and undoped anodes were electrochemically characterized by cyclic voltammetry, electrochemical impedance spectroscopy, and galvanostatic charging-discharging techniques. Interestingly, Y doping at an optimum content of 0.5%mole Y played an important role in a marked improvement in electrochemical properties; ion transport, specific capacity, cell resistance, cycle performance and capacity retention of the nanocomposite anode. All these reasons together make the Y-doped TiO_2(B)/SnO_2 nanocomposite anode a promising candidate for the production of anode electrode materials for high-performance LIBs.

Acknowledgements

The author would like to appreciate the financial support provided by Faculty of Engineering, Prince of Songkla University, Contract No. ENG 62204117S, and the Graduated school of Prince of Songkla University. The authors are thankful to Asst. Prof. Dr. Pipat Chooto and Asst. Prof. Dr. Warakorn Limbut, Faculty of Science, Prince of Songkla University for using electrochemical impedance spectroscopy (EIS). And also wish to acknowledge the Department of Mining and Materials Engineering, Faculty of Engineering, Prince of Songkla University.

References

[1] H. B. Wu, J. S. Chen, X. W. Lou, H. H. Hng. The Journal of Physical Chemistry C. 115(50), 24605 (2011); https://doi.org/10.1021/jp208158m

[2] Y. Liu, Y. Yang. Journal of Nanomaterials. 2016 (2016); https://doi.org/10.1155/2016/8123652

[3] S. Hua, M. X. Jing, C. Han, H. Yang, H. Chen, F. Chen, L. Chen, B. W. Ju, F. Y. Tu, X. Q. Shen, S. B. Qin. International Journal of Energy Research. 43(13), 7296 (2019); https://doi.org/10.1002/er.4758

[4] H. Wang, L. Xi, R. Ma, Z. Lu, C. Y. Chung, I. Bello and J. A. Zapien. Journal of Solid State Chemistry. 190, 104 (2012); https://doi.org/10.1016/j.jssc.2012.02.016

[5] H. Y. Wu, M. H. Hon, C. Y. Kuan, I. C. Leu. Journal of Electronic Materials. 43(4), 1048 (2014); https://doi.org/10.1007/s11664-013-2951-y

[6] X. Yan, Z. Wang, M. He, Z. Hou, T. Xia, G. Liu, X. Chen. Energy Technology. 3(8) 801 (2015); https://doi.org/10.1002/ente.201500039

[7] H. Y. Wu, M. H. Hon, C. Y. Kuan, C. Leu. Ceramics International. 41(8), 9527 (2015); https://doi.org/10.1016/j.ceramint.2015.04.011

[8] J. Ling, C. Karuppiah, M. V. Reddy, B. Pal, C. C. Yang, R. Jose. Journal of Materials Research. 36(20), (2021) 4120; https://doi.org/10.1557/s43578-021-00313-3

[9] M. Aghazadeh, I. Karimzadeh, M. G. Maragheh, M. R. Ganjali. Materials Research. 21 (2018); https://doi.org/10.1590/1980-5373-mr-2018-0094

[10] X. Qu, Y. Hou, M. Liu, L. Shi, M. Zhang, H. Song, F. Du, Results in Physics. 6 1051-1058 (2016); https://doi.org/10.1016/j.rinp.2016.11.021

[11] A. B. Ali Baig, V. Rathinam, J. Palaninathan. Applied Water Science. 10(2), 1 (2020); https://doi.org/10.1007/s13201-020-1143-1

[12] S. Khan, H. Ikari, N. Suzuki, K. Nakata, C. Terashima, A. Fujishima, , K. Katsumata, V. Rodríguez-González. ACS omega. 5(36), 23081 (2020); https://doi.org/10.1021/acsomega.0c02855

[13] P., Choopool, K. Kooptarnond, M. Khangkhamano, V. Rachpech, (2020). Materials Science Forum. 998, 227 (2020); https://doi.org/10.4028/www.scientific.net/MSF.998.227

[14] J. Zhang, J. Guo, H. Xu and B. Cao. ACS Applied Materials & Interfaces. 5, 7893 (2013); https://doi.org/10.1021/am4019884

[15] J. W. Edington. Macmillan International Higher Education. 80 (2016).

[16] J. Liu, J. Wang, Z. Ku, H. Wang, S. Chen, L. Zhang, J. Lin and Z. X. Shen: ACS nano. 10, 1007 (2015); https://doi.org/10.1021/acsnano.5b06275

[17] D. V. Raj, N. Ponpandian, D. Mangalaraj and C. Viswanathan. Materials Science in Semiconductor Processing. 26, 55 (2014); https://doi.org/10.1016/j.mssp.2014.04.003

[18] N. Pineda-Aguilar, M. Sánchez-Domínguez, E. M. Sánchez-Cervantes, L. L. Garza-Tovar. Journal of Materials Research. 35(18), 2491 (2020); https://doi.org/10.1557/jmr.2020.213

[19] O. Cevher and H. Akbulut. Acta Physica Polonica A. 131, 204 (2017); https://doi.org/10.12693/APhysPolA.131.204

[20] W. Wen, X. Yang, X. Wang, L. G. H. Shu, Journal of Solid State Electrochemistry. 19(4) 1235 (2015); https://doi.org/10.1007/s10008-015-2743-9

[21] Y. Liu and Y. Yang. Journal of Nanomaterials. 2016, 1 (2016); https://doi.org/10.1155/2016/2935202

[22] M. S. Park, Y. M. Kang, G. X. Wang, S. X. Dou, H. K. Liu. Advanced Functional Materials. 18(3), 455 (2008); https://doi.org/10.1002/adfm.200700407

[23] S. Khasim, A. Pasha, M. Lakshmi, C. Panneerselvam, A. A. A. Darwish, T. A. Hamdalla, S. Alfadhlia and S. A. Al-Ghamdi, Digest Journal of Nanomaterials & Biostructures. 17(4), 1089 (2022); https://doi.org/10.15251/DJNB.2022.174.1089